Geophys. J. Int. (2012) **188,** 239–252 doi: 10.1111/j.1365-246X.2011.05247.x

Elastic anisotropy of core samples from the Taiwan Chelungpu Fault Drilling Project (TCDP): direct 3-D measurements and weak anisotropy approximations

Laurent Louis,[1*] Christian David,[1] Petr Špaček,[2,3] Teng-fong Wong,[4] Jérôme Fortin[5] and Sheng Rong Song[6]

[1]*Université de Cergy-Pontoise, Cergy, France. E-mail: christian.david@u-cergy.fr*
[2]*Institute of Geophysics, Czech Academy of Sciences, Praha, Czech Republic*
[3]*Masaryk University, Brno, Czech Republic*
[4]*State University of New York at Stony Brook,* NY 11794, *USA*
[5]*Ecole Normale Supérieure de Paris, Paris, France*
[6]*National Taiwan University, Taipei, Taiwan*

Accepted 2011 September 23. Received 2011 September 23; in original form 2011 June 28

SUMMARY

The study of seismic anisotropy has become a powerful tool to decipher rock physics attributes in reservoirs or in complex tectonic settings. We compare direct 3-D measurements of *P*-wave velocity in 132 different directions on spherical rock samples to the prediction of the approximate model proposed by Louis *et al*. based on a tensorial approach. The data set includes measurements on dry spheres under confining pressure ranging from 5 to 200 MPa for three sandstones retrieved at a depth of 850, 1365 and 1394 metres in TCDP hole A (Taiwan Chelungpu Fault Drilling Project). As long as the *P*-wave velocity anisotropy is weak, we show that the predictions of the approximate model are in good agreement with the measurements. As the tensorial method is designed to work with cylindrical samples cored in three orthogonal directions, a significant gain both in the number of measurements involved and in sample preparation is achieved compared to measurements on spheres. We analysed the pressure dependence of the velocity field and show that as the confining pressure is raised the velocity increases, the anisotropy decreases but remains significant even at high pressure, and the shape of the ellipsoid representing the velocity (or elastic) fabric evolves from elongated to planar. These observations can be accounted for by considering the existence of both isotropic and anisotropic crack distributions and their evolution with applied pressure.

Key words: Microstructures; Seismic anisotropy; Acoustic properties.

1 INTRODUCTION

The elastic anisotropy of a porous rock reflects the anisotropic attributes of both the solid matrix and pore space. Bedding in sedimentary rocks, cleavage in slates, preferred orientation of anisotropic minerals and anisotropic distribution of microcracks and pores can all contribute to elastic anisotropy, a seismic manifestation of which is shear wave splitting (Crampin 1981). Even though analysis of elastic wave propagation in an anisotropic medium can be highly complex, the investigation of this phenomenon has evolved to become a useful tool for deciphering rock physics attributes in a geologic formation, especially when the anisotropy is relatively weak which would allow the analysis to be simplified (Helbig & Thomsen 2005).

Extensive laboratory studies have been conducted on the elastic or seismic anisotropy of different rock types (Lo *et al*. 1986; Hornby 1998). These studies show that seismic anisotropy at elevated pressures arises primarily from lattice preferred orientation (Kern 1993; Johnston & Christensen 1995), whereas at relatively low pressures it is usually controlled by the presence of an oriented system of open microcracks, which may develop as a result of rock forming processes or tectonic deformation. Indeed Nur & Simmons (1969) demonstrated in a seminal study the correspondence among seismic anisotropy, stress-induced cracking and orientations of the applied stress field.

In 1999 the M_w 7.6 Chi–Chi earthquake resulted in significant casualty and damage (Shin & Teng 2001). Its main rupture along the Chelungpu fault system was associated with surface break extending >100 km. The Taiwan Chelungpu-fault Drilling Project (TCDP) was undertaken to drill into this thrust fault, with the overall research goal to gain fundamental understanding of the physics

*Now at: BP America, Subsurface Technology, Houston, USA.

of earthquakes and faulting. Vertical drilling of Hole A at Takeng to a depth of 2 km through the northern portion of Chelungpu fault was completed in 2004. In a previous study, Louis *et al*. (2008) investigated the elastic and magnetic anisotropies of a total of 15 core samples retrieved from TCDP Hole A at depths ranging from 589 to 1412 m. They systematically characterized the anisotropies of *P*-wave velocity (APV) and magnetic susceptibility (AMS) as functions of depth and porosity. Microstructural observations were also conducted so as to establish possible correlations between the anisotropic properties and the petrofabrics induced by tectonic deformation and stress field.

The sonic velocity measurements were conducted following the protocol of Louis *et al*. (2004). For each available core a triplet of cylindrical plugs were drilled along three perpendicular directions. The velocity anisotropy of each plug was characterized by measuring the traveltimes for *P*-wave propagation across the mid-section along 8 diameters at an angular interval of 22.5°. For a weakly anisotropic rock, they demonstrated that data for the APV of the three orthogonal plugs can be approximated by a second-rank velocity tensor. Since the magnetic susceptibility is also described by a second rank tensor (Nye 1957), this provides a common basis for comparison of elastic and magnetic anisotropies as well as their relations to microstructure.

With reference to Thomsen's (1986) and Tsvankin's (1997) results for a weakly anisotropic rock, Louis *et al*. (2004) argued that the APV data of most sedimentary rocks can be approximated by a second rank tensor with an error of <4 per cent. A primary objective of this study is to assess the validity of this approximation, by comparing with direct measurement of the 3-D anisotropy in a spherical sample under confinement using a specially designed apparatus at the Geophysical Institute of Prague. The apparatus has been used to acquire relatively comprehensive data on APV of samples from a variety of geological settings (Pros *et al.* 1998b; Vajdova *et al.* 1999; Pros *et al.* 2003; Machek *et al*. 2007; Vilhelm *et al.* 2008). Similar measurements on spheres have also been undertaken at Institut Français du Pétrole, with a focus on microcrack-induced anisotropy (Arts *et al.* 1994, Rasolofosaon *et al.* 2000) and its relation to permeability anisotropy (Rasolofosaon & Zinszner 2002).

However preparation of a spherical sample is quite cumbersome, and in contrast, the tensorial method of Louis *et al.* (2004) is relatively straightforward to implement, as long as core samples in three mutually orthogonal orientations are available and the anisotropy is relatively weak so that the approximation is valid. Our objective in this work is first to compare direct *P*-wave velocity anisotropy measurements on spheres to the prediction of the tensorial method of Louis *et al.* (2004), secondly to provide a microstructural interpretation for the observed pressure dependence of the measured properties which complements the work of Louis *et al*. (2008) on core samples from the same TCDP borehole.

2 SAMPLING AND METHOD

2.1 TCDP overview and core locations

The main rupture of the 1999 Chi–Chi earthquake was located along the Chelungpu fault system (Fig. 1a), with surface rupture extending over 100 km and uplifts of 8 m in some locations. The vertical drilling of TCDP Hole A in 2004 through the northern portion of Chelungpu fault at Takeng (near the city of Taichung) reached a depth of 2 km. Total recovery of the mostly continuous cores from TCDP Hole A was about 97 per cent (Song *et al*. 2007). At least three stratigraphic sequences oriented N15–30E could be identified from the TCDP core samples (Fig. 1b): the Cholan formation (late Pliocene to early Pleistocene), the Chinshui shale formation (Pliocene) at depth 1027–1268 m, the Kueichulin formation (late Miocene to Pliocene) down to 1712 m, and the

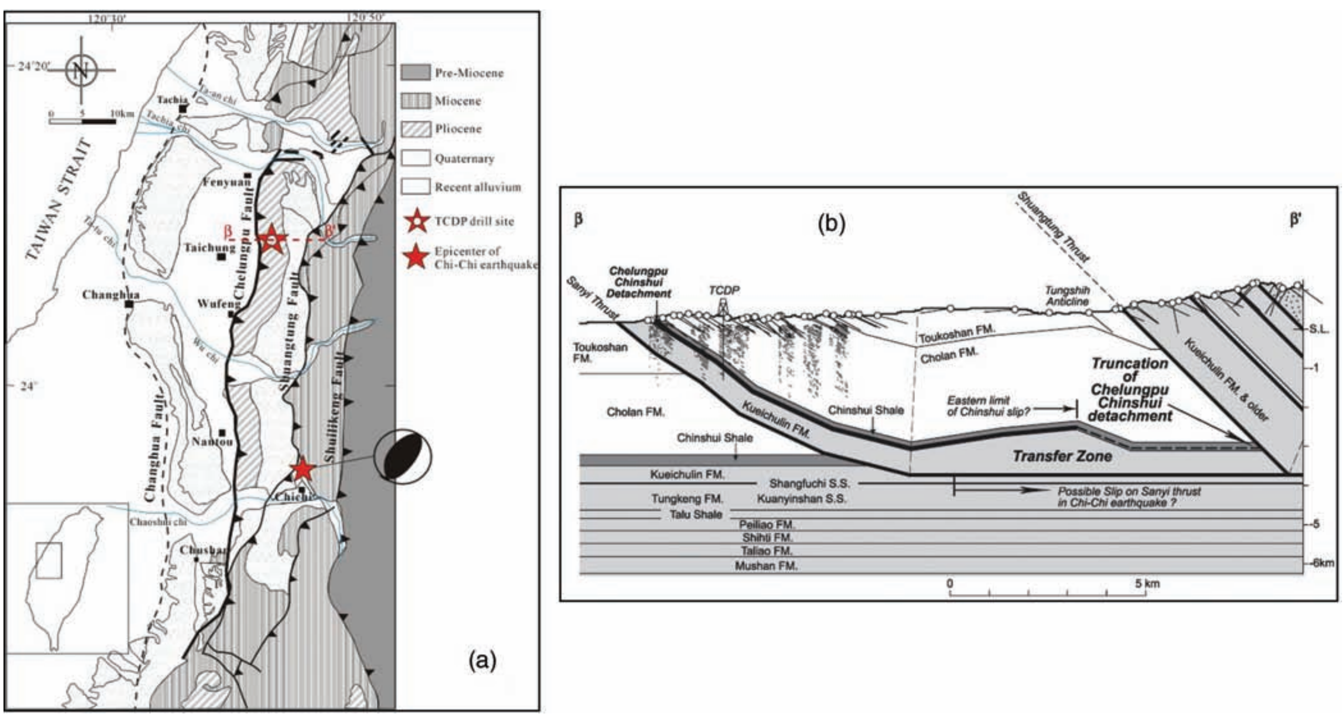

Figure 1. (a) Map of Eastern Taiwan with the location and focal mechanism of the 1999 ChiChi devastating earthquake. The TCDP drill site is also indicated in the northern part of the fault zone. (b) Vertical cross section showing the geological formations involved in the Chelungpu thrusting. Again the TCDP drill hole reaching the major fault zone is shown.

Cholan formation again at depths below 1712 m. The Cholan formation at the top is characterized by thick sandstone layers and alternating sandstone–siltstone–mudstone layers with weak to intense bioturbations. The sandstone is predominately made up of quartz and slate fragments, with some feldspar, sandstone quartzite fragments and clay matrix. The Chinshui formation is primarily made up of siltstone, with subsidiary thin layers of fine-grained sandstone, mudstone and alternating layers of sandstone and siltstone. The Kueichulin formation is made up of thick sandstone layers, with subsidiary thin layers of siltstone and shale. Structural and deformation features indicate the existence of several fracture zones in the Chinshui shale formation with one particular at 1111 m depth considered to be the plausible location that underwent significant slip during the Chi–Chi earthquake (Song *et al*. 2007).

The 15 core samples investigated by Louis *et al*. (2008) were retrieved from TCDP Hole A at depths ranging from 589 to 1412 m, including six sandstones and nine siltstones, on which the anisotropy of magnetic susceptibility and *P*-wave velocity was analysed. They concluded that the directions of anisotropy for magnetic susceptibility were consistent for both sandstones and siltstones, and could be related to the regional stress regime, whereas an additional contribution of anisotropy for the *P*-wave velocity was detected only in the sandstones, which could be related to the existence of an anisotropic crack distributions at the grain scale as revealed by quantitative characterization of three samples (#04, #09 and #14). For this study, we investigated the velocity anisotropy of three spherical sandstone from the following depths: 850 m (in the proximity of sample #04 in the Cholan formation), 1340 m and 1365 m (in the proximity of sample #09 in the Kueichulin formation).

2.2 3-D measurement on spherical samples

Velocity measurements on spherical dry samples were conducted using the experimental facilities at the Geophysical Institute of Prague described by Pros *et al*. (1998a). A schematic view of the experimental setup is shown in Fig. 2(a). It is based on the classical pulse transmission method using two ultrasonic transducers, one transmitter (T), one receiver (R), mounted on a frame which can rotate about two perpendicular axes (Fig. 2b) defining the angles λ (longitude) and ϕ (latitude). This allows one to attach the two transducers at diametrically opposite locations in virtually any direction in space, except near the vertical direction where the sample is firmly clamped. Typically an angular step ($\Delta\phi$ or $\Delta\lambda$) of 15° is imposed in the latitude and longitude, which would allow one to acquire a total of 132 independent measurements. Confinement of this experimental device inside a pressure vessel allows one to characterize the velocity anisotropy at confining pressures ranging up to 400 MPa. To prevent the confining fluid from penetrating into the rock, the spherical sample (50 mm in diameter) is encapsulated in a thin epoxy resin film (0.05 mm thickness). Both ultrasonic transducers have a resonance frequency of 2.5 MHz. A pulse generator is connected to the transmitter, and the signal recorded by the receiver is sent to a digital oscilloscope with a 100 MHz sampling rate. Only 40 μs of the transmitted signals are stored for the

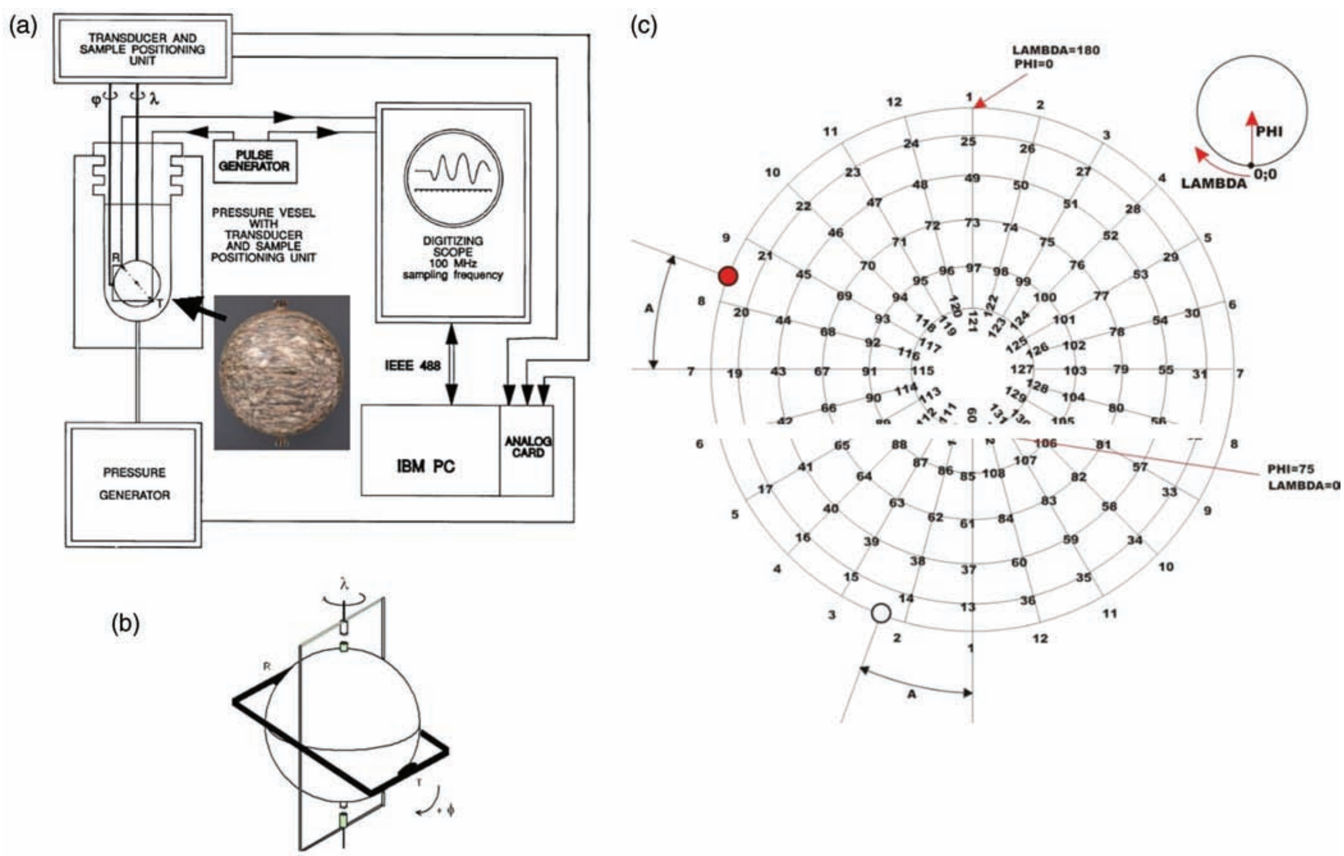

Figure 2. Sphere method: (a) Schematic representation of the experimental system for measuring the *P*-wave velocity anisotropy on spheres under confining pressure. (b) Vertical and horizontal rotating frames where the ultrasonic transducers are implemented. (c) Stereonet corresponding to lower hemisphere equal area projection of directions defined on the sphere with angular steps of 15° in latitude and longitude. (a and b modified from Pros *et al*. 2003)

analysis, which is considered to be long enough for picking the first arrival.

To visualize the 3-D data set for the angular distribution of *P* velocity at each pressure level, we will use a 2-D stereonet that corresponds to a lower hemisphere equal-area projection (Schmidt stereonet). The correspondence with the (λ, ϕ) coordinate system is illustrated in the inset schematic diagram in Fig. 2(c), and orientations for the 132 measurements have been labelled in the stereogram. The solid red circle corresponds to the upward vertical direction that is along the axis of the cylindrical core retrieved from the TCDP hole. The strike of the bedding plane (N15E horizontal direction) is indicated by the open circle. Accordingly the centre of the stereonet corresponds to the N105E horizontal direction.

2.3 Tensorial method on three orthogonally cored samples

The experimental configuration used by Louis *et al.* (2003, 2004) is illustrated in Fig. 3. It is necessary to have a good spatial distribution of measuring directions to correctly characterize the anisotropy, and this can be achieved by measuring the *P*-wave velocity across several diameters in three samples cored in mutually orthogonal directions from one single block (Fig. 3a). An optimized angular measuring scheme was proposed as shown in Fig. 3(b). As for the measurements on spheres, a classical setup for acoustic properties is used, including a pulse generator, two ultrasonic transducers with a resonance frequency of 0.5 MHz, and a digital oscilloscope connected to a PC for data acquisition and analysis. For each measurement the piezoelectric transmitter and receiver are located in opposite positions across a diameter on the circular surface of the sample, and the time of flight of the *P* wave is measured. This is repeated eight times per sample after rotating it with an angular shift of 22.5°. The velocity profiles obtained for the three orthogonal samples are then corrected from slight variations in density from sample to sample (Louis *et al*. 2004), and the set of 24 measurements provides traveltimes along 21 independent orientations uniformly distributed in three orthogonal planes. Accounting for the errors associated with picking the first arrival and measuring the sample diameter, the standard error for the measurements is about 0.03 km s^{-1} (Louis *et al*. 2003).

Louis *et al.* (2004) showed that most sedimentary rocks can be modelled as transversely isotropic rocks such that the *P*-wave velocity V_P as a function of θ, the angle between the axis of symmetry and the direction of propagation, can be fitted with an error of less than 4 per cent by the equation

$$V_P = V_o \left(1 + \kappa . \sin^2 \theta\right), \tag{1}$$

where V_o is the *P*-wave velocity in the direction perpendicular to the isotropic plane, and κ is the anisotropy parameter in the tensor approach. With reference to Thomsen's (1986) expression for weak anisotropy

$$V_P = V_o \left(1 + \delta . \sin^2 \theta + (\varepsilon - \delta) . \sin^4 \theta\right) \tag{2}$$

this implies that the rock can be approximated as 'elliptically anisotropic', with the Thomsen anisotropy parameters ε and δ being equal such that *P* wave fronts emanating from a point source are elliptical in shape (in any plane containing the symmetry axis of the transversely isotropic rock). The approximation in eq. (1) would also imply that the velocity can be described by a symmetric, second rank tensor V_{ij}, so that the *P*-wave velocity for propagation in the direction of unit vector **n** is simply given by

$$V_P = V_{ij} \mathrm{n}_i \mathrm{n}_j . \tag{3}$$

Since Thomsen's analysis has been generalized by Tsvankin (1997) from a transversely isotropic to an orthotropic material, Louis *et al.* (2004) concluded that the *P*-wave anisotropy in any weakly anisotropic rock can generally be approximated by such a symmetric, second rank tensor. Accordingly, they proposed a methodology whereby the laboratory data of *P*-wave velocity in multiple directions are fitted to eq. (3) to find the ellipsoidal envelope of the representation quadric, as well as the directions and magnitudes of the three principal axes defined by the eigenvectors and eigenvalues of this symmetric tensor (Fig. 3c). Our elliptical anisotropy best fit given by the eigenvalues of a second rank symmetric tensor that produce the best fit with the measured data in the least-squares sense by no means represents the best fit in terms of the approximate stiffness tensor as compared to the true observed one, as rigorously derived by Sevostianov & Kachanov (2008).

The six independent tensor elements V_{ij} are calculated from the 21 independent velocities measured on diameters with known orientations by a least-squares inversion method. Eigenvalues and eigenvectors are then obtained by diagonalization of the velocity tensor and can be represented in 3-D on an ellipsoid (Fig. 3c). By convention we will call V_1 the eigenvector with maximum magnitude, V_2 the eigenvector with intermediate magnitude and V_3 the eigenvector with minimum magnitude. The advantage of the tensorial approach is that, first, it is simpler than estimating the elastic fourth rank tensor from which the velocities must theoretically be derived

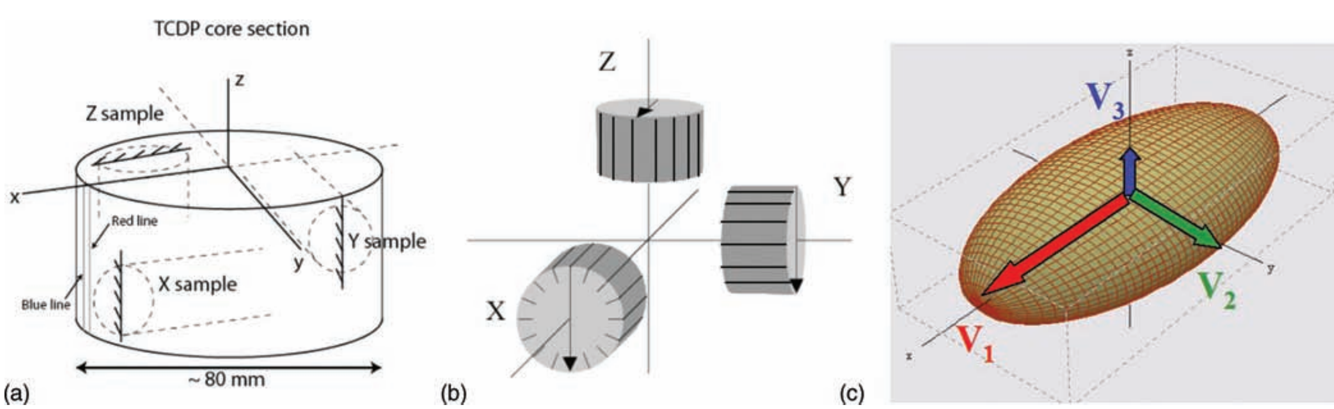

Figure 3. Tensor method: (a) Coring scheme with three orthogonal samples are cored from a large core retrieved at depth. (b) The three samples with the angular sampling for the measurements on diameters. (c) Schematic view of a 3-D ellipsoid used to represent the second-rank pseudo tensor for *P*-wave velocities.

(Mavko *et al.* 1998), and secondly, the velocity tensor can conveniently be compared to any other second rank tensor representing other physical properties like permeability, electrical conductivity or magnetic susceptibility (e.g. David *et al.* 2007). To represent the 3-D orientation of the velocity eigenvectors, one can use a 2-D stereonet like for the sphere measurements.

3 RESULTS

We first present and discuss the measurements obtained on the spherical sample in terms of anisotropy and compare those results to the prediction of the tensorial approximation. Then we focus on the pressure dependence of *P*-wave velocity and anisotropy up to 200 MPa also obtained in the same experiments on the spherical samples.

3.1 Velocity anisotropy measured on spherical samples

We plotted in Fig. 4 the results of the sphere measurements for the three sandstone samples from cores retrieved at depths 850, 1365 and 1394 m, at six different confining pressures: 5, 10 and 20 MPa on Fig. 4(a); 50, 100 and 200 MPa on Fig. 4(b). For each pressure, the stereonets on the left correspond to the raw velocity measurements in the 132 different directions investigated in the sphere analysis,

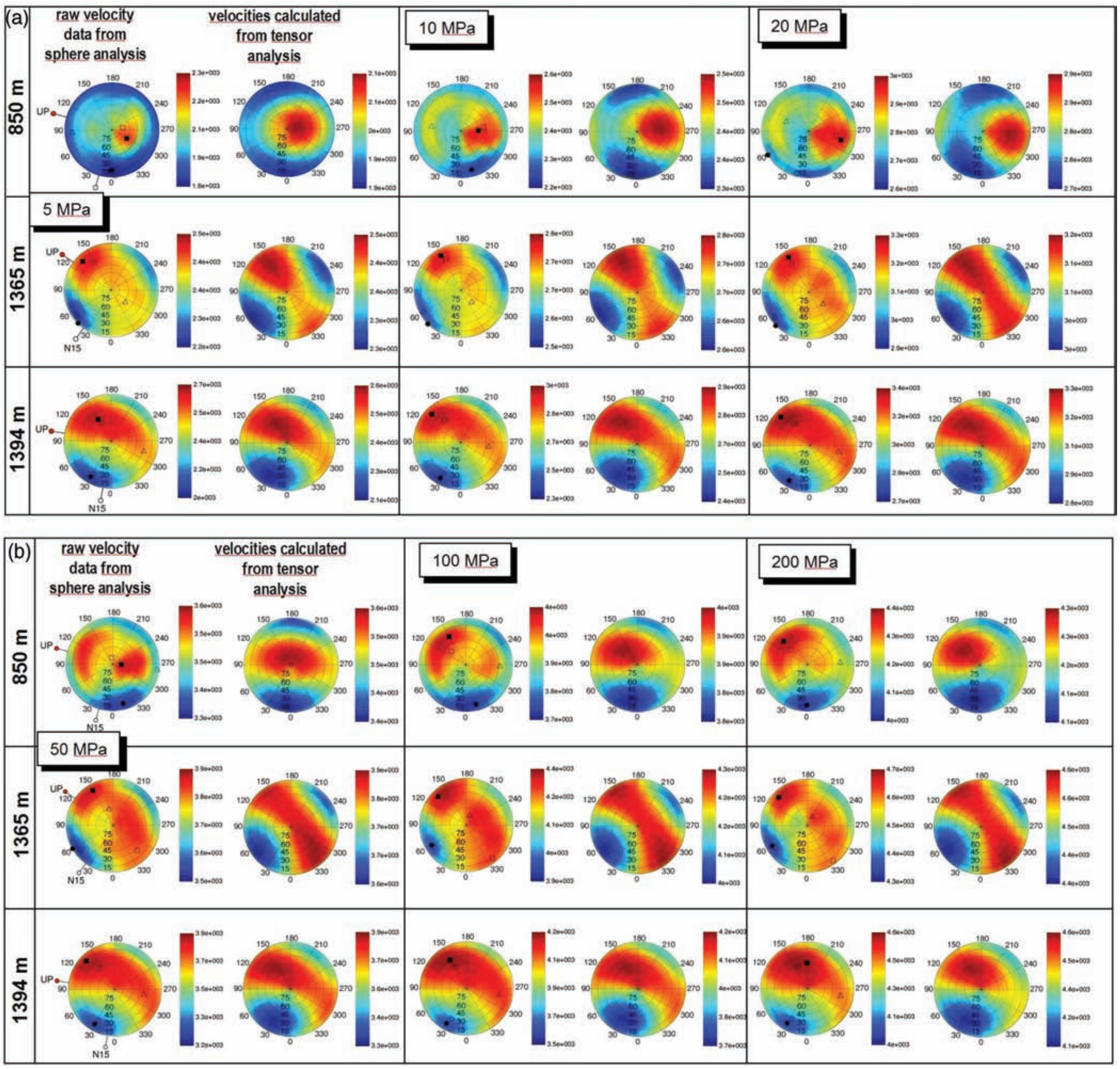

Figure 4. Comparison of the raw *P*-wave velocity measurements in 132 different directions and the prediction of the tensor method for the three samples at 850, 1365 and 1394 m depth, at different confining pressures. For each pressure the stereonets on the left are the raw measurements with the specified colour coding. Solid symbols are the maximum (square) and minimum (circle) velocities, Open symbols are the eigenvectors of the velocity tensor obtained by a least-square method from the raw velocity data (open triangle is for intermediate eigenvector). (a) Confining pressures from 5 to 20 MPa. (b) Confining pressures from 50 to 200 MPa.

which correspond to an angular sampling of 15° in latitude and longitude. As explained above the directions are represented on an equal area lower hemisphere projection. The colour scale next to the stereonet indicates the range of velocities measured in each sample. The range of measured velocities is quite large, from 1900 m s^{-1} at low pressure up to 4600 m s^{-1} at the highest pressure. Note that the colour scale is kept constant and systematically adjusted to the extreme velocity values, therefore the velocity scale for a given sample is not exactly the same from one pressure to the other. The solid squares show the location of the maximum velocity measured $V_{\max}$, and the solid circle where the minimum velocity $V_{\min}$ was found.

The measurements were made on the intersections of the 15° × 15° angular grid, and the stereonet is made up of 60 quadrilateral elements that surround a central, circular element (Fig. 2c). To each quadrilateral element we assigned a constant velocity equal to the arithmetic mean of the velocities measured along the four adjacent nodes. The centre of the projection, which corresponds to the direction along which the sample is clamped, was attributed the average velocity of the 12 surrounding nodes. After each element was assigned a value, a light Gaussian smoothing was finally applied to facilitate observation. This operation did not affect the colour scale extrema since the filter radius was smaller than the half-length of the elements.

On the stereonets, for the spherical sample data acquired at the lowest pressure (5 MPa), the solid red circle marks upward vertical direction and the open circle marks the strike of the bedding plane (N15E horizontal direction). As can be seen there is a good agreement for our three samples between the location of minimum velocities on the stereonet and the position of the bedding strike, in agreement with the series of room pressure measurements of Louis *et al.* (2008) on many TCDP sandstone samples using the tensor method.

Let us next describe briefly the evolution of the directions of maximum and minimum measured velocity. If we look at the colour patterns, it is clear that for both samples at 1365 m and 1394 m the overall velocity distribution is pretty the same for all the pressure range and the position of maximum and minimum velocities (solid symbols) do not change significantly with increasing pressure. A slightly different picture is obtained for the sample at 850 m where at low pressure the dominant colour on the stereonet is blue, then evolves towards dominant red tones at higher pressure. This change in colour is associated with a rotation of the velocity maximum. For the three samples, the orientation of the minimum velocity direction remains stable, except for sample at 850 m and 20 MPa confining pressure where the minimum rotates by about 60° in azimuth, although the location of the larger low velocity sector remains consistent with the ones at other pressures. For samples at 1365 m and 1394 m, the maximum velocity direction also remains fairly stable across the pressure range. In the sample at 850 m, two distinct high velocity zones are sequentially observed upon pressurization with a transition at 50 MPa. As discussed later, this observation suggests the participation of several sources of anisotropy, of which one at least is pressure dependent. Note also that, as they result from measurements, the directions of maximum and minimum velocities are not necessarily orthogonal, in contrast with the principal directions implicitly assumed in the tensor analysis.

3.2 Prediction of second rank tensor approximation

The velocity versus orientation data set obtained on the spherical samples was used as input data for the tensor method described above. The velocity tensor defined in eq. (3) is built, and the eigenvalues and eigenvectors are calculated using a least-squares scheme (Louis *et al.* 2004). The maximum and minimum velocity values obtained with the tensor approximation are given in Table 1 for comparison with the direct measurements. We also provide for each pressure step a residual value that corresponds to the average of the differences between direct measurements and values recalculated from the best-fitting tensor. In Fig. 4 the directions of the three eigenvectors, necessarily orthogonal, are plotted as open symbols on the same stereonets as the measured velocities for comparison. The open square correspond to the eigenvector with maximum amplitude V_1, the open circle to the one with the smaller amplitude V_3 and the open triangle to the intermediate eigenvector V_2. Looking at the spatial location of these eigenvectors with respect to the measured maxima and minima velocities, we can see that in general there is a good agreement between the orientation of measured and predicted velocity extrema. On the average, the discrepancy is of the order of the width of the angular sectors, say $+/-$ 15° which is rather good. To go further in the comparison between measured and predicted values, the stereonet plotted on the right next to the measured data represents for each pressure the predicted velocity data field calculated at each location where a measurement was done on the spheres. Therefore if the tensor approach provides a valid description of the actual velocity anisotropy, the distribution of colours in adjacent stereonets should be similar (although the velocity scale might slightly change as mentioned above). In general we observe a very good agreement between the prediction of the tensorial approach and the measured values, for the three different samples, at all the pressures: this gives us some confidence in our assumption that velocity anisotropy in rocks can be approximated by a second-rank tensor.

The results from the tensor approximation may also be compared with what was obtained by Louis *et al.* (2008) at virtually ambient pressure condition in the same samples. Fig. 5 is a stereoplot taken from Louis *et al.* (2008) showing in grey the eigenvectors obtained for all of their sandstone samples in the geographic reference. We overlay on the same figure the maximum and minimum velocity directions obtained from the direct measurements on spheres (solid symbols) at 5 MPa, and the directions corresponding to the three eigenvectors obtained with the tensor approximation (open symbols). As compared to Fig. 4, the directions have been rotated to fit the geographic reference. First, the location for the minimum velocity direction is very well constrained overall, with an N15 subhorizontal orientation parallel to the strike of the bedding. For the maximum and intermediate velocity directions, two observations can be made. First, the maximum velocity directions generally scatter within the plane perpendicular to the average minimum velocity direction, which is standard for the tensor-derived vectors (open squares) but not forced as far as the direct measurements are concerned (solid squares). Secondly, while the tensor-derived maximum and intermediate velocity directions are a good match for samples at 850 m, a poorer match is observed between maximum and intermediate velocity directions for the two other samples (1365 m and 1394 m) as compared to the results of Louis *et al.* (2008). This discrepancy, which will be addressed in the discussion section, can be associated with the two independent observations that (1) there is a 5 MPa difference in confining pressure between the two data sets, and (2) as can be seen in Fig. 4(a), the plane within which intermediate and maximum velocity values are located is nearly isotropic, and therefore unlikely to result in well constrained positions for the eigenvectors. It is worth mentioning here that this nearly isotropic plane matches exactly the orientation

Table 1. Maximum and minimum velocities ($V_{\max}$, $V_{\min}$) measured on the sphere samples for each pressure step with corresponding anisotropy factor, and predicted values derived from the tensor approach (V_1, V_3) with anisotropy parameters P_j and T_j and average residuals.

		3-D Measurements			Tensor analysis						
Sample	Pressure (MPa)	$V_{\max}$ (m s^{-1})	$V_{\min}$ (m s^{-1})	Total anisotropy (per cent)	V_1 (m s^{-1})	V_2 (m s^{-1})	V_3 (m s^{-1})	Total anisotropy (per cent)	P_j	T_j	Average residual (m s^{-1}; per cent)
850	3	2267	1625	34.2	2076	1770	1713	19.6	1.23	−0.66	74.4; 3.96
	5	2285	1825	22.9	2143	1942	1852	14.7	1.16	−0.35	48.8; 2.43
	10	2595	2209	16.0	2509	2385	2297	8.8	1.09	−0.16	51.7; 2.15
	15	2831	2437	15.1	2721	2581	2514	8.0	1.08	−0.34	49.7; 1.90
	20	2974	2638	11.9	2931	2787	2718	7.6	1.08	−0.34	44.3; 1.59
	35	3357	3053	9.4	3292	3240	3105	5.8	1.06	0.46	41.7; 1.29
	50	3613	3314	8.6	3568	3502	3365	5.8	1.06	0.37	42.7; 1.22
	100	4047	3721	8.3	4005	3916	3774	5.9	1.06	0.24	43.3; 1.11
	200	4365	4001	8.6	4339	4213	4077	6.2	1.06	0.06	32.7; 0.77
	100	4068	3724	8.8	4045	3921	3777	6.9	1.07	0.09	37.5; 0.96
1365	0.1	2081	1570	26.9	2048	1929	1664	20.4	1.24	0.42	44.8; 2.39
	1	2191	1784	20.2	2111	2017	1917	9.6	1.10	0.05	34.4; 1.71
	5	2537	2175	15.1	2483	2418	2259	9.4	1.10	0.44	30.1; 1.27
	10	2829	2483	12.9	2764	2713	2560	7.6	1.08	0.51	23.4; 0.87
	20	3265	2860	13.0	3200	3170	2958	7.8	1.09	0.76	31.7; 1.02
	50	3910	3536	9.9	3863	3840	3626	6.3	1.07	0.81	33.4; 0.89
	100	4363	3853	12.1	4318	4278	4006	7.4	1.09	0.75	38.2; 0.91
	200	4706	4251	10.0	4642	4602	4372	5.9	1.07	0.71	39.8; 0.88
	100	4414	4008	9.5	4353	4309	4130	5.2	1.06	0.61	35.6; 0.84
1394	0.1	1987	1375	36.6	1913	1681	1346	34.5	1.43	0.26	42.7; 2.58
	5	2678	2029	26.5	2651	2504	2119	21.9	1.26	0.49	41.9; 1.75
	10	2980	2324	24.0	2929	2816	2412	19.0	1.23	0.60	39.0; 1.46
	20	3375	2663	22.7	3349	3242	2789	17.9	1.22	0.65	42.0; 1.37
	50	3915	3151	20.8	3885	3770	3292	16.2	1.19	0.64	41.4; 1.15
	100	4240	3500	18.4	4230	4117	3674	13.9	1.16	0.62	43.2; 1.10
	200	4601	3999	13.7	4616	4432	4122	11.2	1.12	0.28	34.3; 0.79
	100	4452	3756	16.5	4438	4260	3908	12.6	1.14	0.36	36.8; 0.88

Note: the grey-shaded lines contain data plotted in the equal area projections (common pressures).

of the network of parallel microcracks observed by Louis *et al.* (2008).

3.3 Pressure dependence of velocity and anisotropy

Let us now focus on the pressure dependence of *P*-wave velocity in the tested rock samples. Again we will compare the measured data and the results predicted by the tensor approximation, focusing on the maximum and minimum velocities. In Fig. 6(a) we plotted for each sample the evolution of the maximum ($V_{\max}$) and minimum ($V_{\min}$) velocities measured on the spheres (solid squares and circles, respectively) as well as the maximum (V_1) and minimum (V_3) eigenvalues given by the model (open squares and circles, respectively) as a function of applied pressure. The red symbols correspond to the eigenvalues derived from measurements on three orthogonal core samples at the same depth under room conditions: these data come from our previous study on TCDP samples (Louis *et al.* 2008) and are in very good agreement with the measurements on spheres at the lowest confining pressure. Note that the data of Fig. 6 provides the results obtained for all pressure steps (see Table 1) and not only the ones plotted in Fig. 4. As expected the *P*-wave velocity increases with applied pressure due to progressive compaction and crack closure, a well-known observation (e.g. Mavko *et al.* 1998). At the highest-pressure steps (100–200 MPa) the increasing trend is still present although with a milder slope, showing that there are still cracks remaining open. After completion of the loading stage, the samples were unloaded and another measurement was made at 100 MPa confining pressure (the stereonet is not shown for this unloading stage). We can see in Fig. 6(a) that for most of the samples the velocity after unloading is higher than in the loading stage. This is particularly true for the sample cored at the highest depth, where irreversible compaction and/or crack closure makes the velocity at 100 MPa be 10 per cent higher after unloading. Again, like for the spatial distribution of velocities (Fig. 4), there is a very good agreement between the pressure dependent magnitude of maximum and minimum velocities, and the magnitudes retrieved by the tensor approach. In Fig. 6(b) we plotted the *P*-wave anisotropy parameter *A* defined as

$$\mathrm{A(per\ cent)} = 200\,(\max(V_P) - \min(V_P))\big/(\max(V_P) + \min(V_P)), \quad (4)$$

where $\max(V_P)$ and $\min(V_P)$ represent either the maximum and minimum velocities measured on the spheres, or the maximum and minimum eigenvalues estimated by the tensor approximation (see also Table 1). The initial value at low pressure is compared to the one found by Louis *et al.* (2008) on three orthogonal cylindrical samples (red circle): whereas a good agreement is found for the sample at 850 m, there is a discrepancy of +/−15 per cent in absolute values for the other samples. As pressure increases, the *P*-wave anisotropy decreases sharply from an initial value close to 30–35 per cent, then flattens to become almost constant at a value

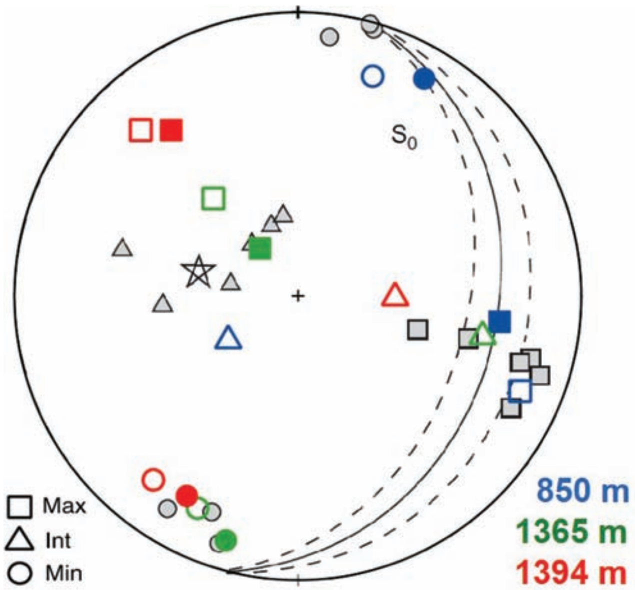

Figure 5. Principal directions derived from the tensor analysis for the three samples at 850, 1365 and 1394 m depth (open symbols) at 5 MPa compared to the extrema velocities measured on the spheres (solid symbols) and the directions found by Louis *et al.* 2008 (grey symbols). The star indicates the orientation of the bedding pole, the inclined plane correspond to the bedding plane (plain line) with $+/-$ 10° uncertainty (dashed lines).

of about 10 per cent for pressures higher that 20 MPa. There is therefore a large change in anisotropy by a factor 3, and a residual anisotropy at the highest pressure, which persists after unloading. Comparing the measured and the predicted anisotropy, we can see in Fig. 6(b) that the predicted results are systematically lower than the measured data, with an almost constant shift by about 5 per cent in absolute value. Tentatively we explain this discrepancy by the fact that the values predicted by the tensor analysis are smoother than the raw data set which is sensitive to local heterogeneities: milder contrasts between extreme values should then be expected from the tensor approximation, leading to a reduced anisotropy. However the shape of the anisotropy decreasing trend is preserved and compares satisfactorily with the measured data.

In Fig. 7 we analysed in more details our predicted directional results using the so-called P_j/T_j plot which compares the corrected degree of anisotropy P_j to the shape parameter T_j (Jelinek 1981), two parameters which depend on the velocity eigenvalues, and which definition can be found in our previous work (Louis *et al.* 2008). Typically, P_j is a measure of the sphericity of the ellipsoid (with $P_j \geq 1$, with $P_j = 1$ for a perfect sphere), and T_j is the shape parameter taking negative values ($-1 < T_j < 0$) when the fabric is elongated in one direction and positive values ($0 < T_j < 1$) when the fabric is planar (Jelinek 1981). When $T_j = 0$, the ellipsoid is said ‘triaxial’, meaning that the ratio between maximum and intermediate eigenvalues is identical to the one between intermediate and minimum eigenvalues. The use of these parameters, which is fairly extensive in magnetic susceptibility studies (e.g. Tarling & Hrouda 1993; Borradaile & Henry 1997), may inform on the amount, shape and/or distribution of the elements responsible for the measured signal, which can be in some cases compared with the finite strain ellipsoid. Starting from the initial values at room conditions (solid symbols) obtained on core samples by Louis *et al.* (2008), the anisotropy parameter P_j decreases while the shape parameter T_j globally increases when the confining pressure is raised up to 200 MPa. The decrease in P_j basically repeats what was shown in Fig. 6(b), with the difference that here the anisotropy is calculated using the three eigenvalues as opposed to the maximum and minimum ones only. The global increase in T_j shows that for the three samples, the *P*-wave velocity fabric becomes more planar as pressure increases, which suggests changes in the relative contributions of the microstructural sources of anisotropy, and more specifically an enhanced contribution of the set of parallel microcracks observed by Louis *et al*. (2008). A closer look at the evolution of T_j with pressure shows that a decrease seems to occur at higher pressure steps, which at least for the sample at 850 m seems to reflect the displacement of the maximum velocity zone in Figs 4(a) and (b), although irrecoverable mechanical deformation past 50 MPa cannot be ruled out.

4 DISCUSSION AND CONCLUSION

We have shown that the data set of *P*-wave velocity measured in 132 independent directions on dry spherical samples machined in TCDP samples cored at three different depths can reasonably well be described by the tensorial method proposed by Louis *et al*. (2003, 2004). Furthermore, the directions of anisotropy are in good agreement with the previous results obtained by Louis *et al*. (2008) on a larger set of core samples. Let us first discuss the validity of the tensorial method for describing *P*-wave velocity anisotropy, then we intend to give an interpretation of our results in terms of microstructure on the basis of theoretical models for the pressure dependence of seismic properties.

4.1 VALIDITY OF THE TENSORIAL APPROACH FOR DESCRIBING *P*-WAVE VELOCITY ANISOTROPY

As mentioned earlier, the rationale for using a simple tensorial method for *P*-wave velocity anisotropy, such as presented in Louis *et al.* (2003, 2004) on various core samples, is the possibility of describing efficiently the full 3-D velocity anisotropy using a limited number of measurements (as low as 6, minimum required for calculating a second-order symmetric tensor), hence of incorporating the richness of *P*-wave velocity data into structural studies along with other tools such as the anisotropy of magnetic susceptibility. Although such an approach would obviously prove to be wrong in the case of a monocrystal, we demonstrate here that a geologically processed aggregate does present anisotropy characteristics, which are necessarily related to a certain extent to experienced stresses and strains.

In our comparison between thorough *P*-wave velocity measurements on spheres and their tensorial best fit, we showed that overall we were able to recover a large portion of the original information. First the locations of the maximum and minimum velocity directions were preserved through the tensorial analysis (Fig. 4). Secondly, the general picture of the velocity magnitudes were also very well reproduced, including the anisotropies and their evolution across pressure steps, despite a slight misfit explained by a smoothing effect of the tensorial approach on the extreme measurements (Figs 4 and 6). Finally, in terms of geological significance, we showed that the results obtained from the spheres are virtually identical to the ones obtained with the tensorial method by Louis *et al.* (2008), with a very well constrained location for the minimum velocity direction, and a slight mismatch between the other principal directions which might be related to pressure effects (Fig. 5). It is useful to recall here that,

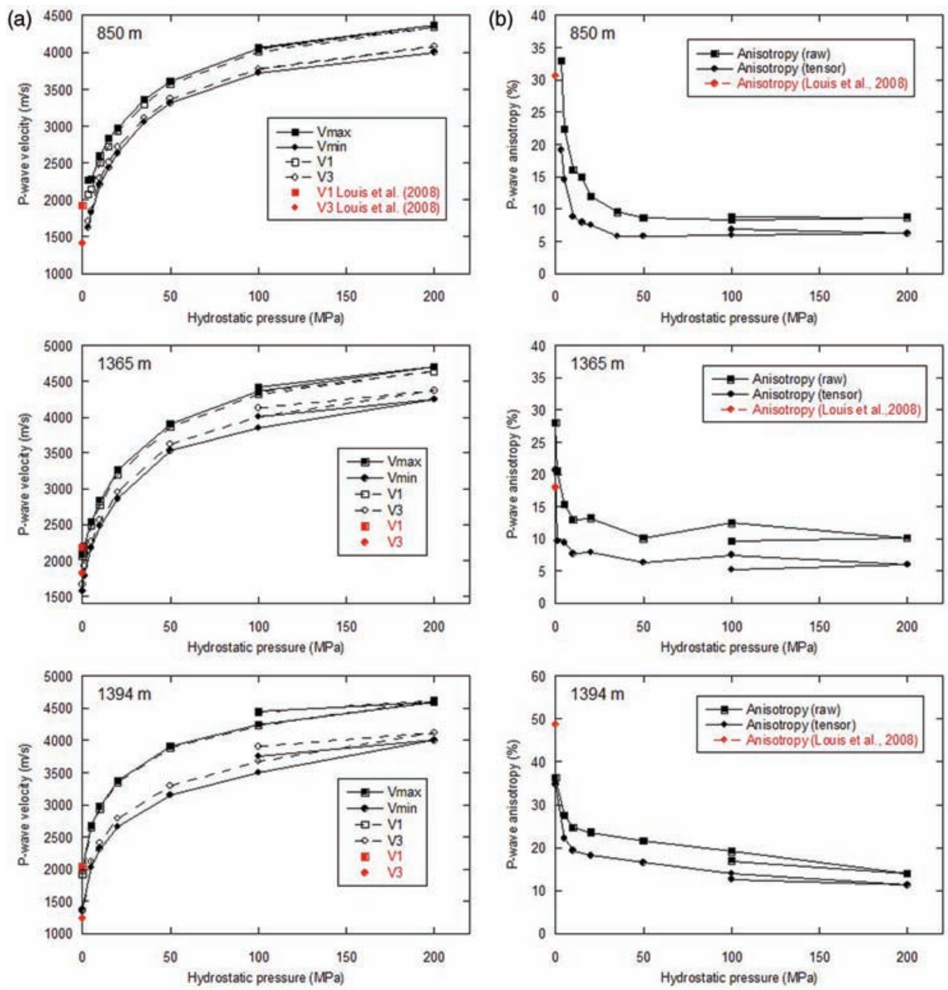

Figure 6. (a) Evolution of maximum and minimum *P*-wave velocities measured on spheres (solid symbols), and maximum and minimum eigenvectors derived from tensor analysis (open symbols with confining pressure. (b) Evolution of measured and derived *P* wave anisotropies versus confining pressure. The value obtained by Louis *et al.* (2008) for TCDP samples at similar depths is plotted in red for comparison.

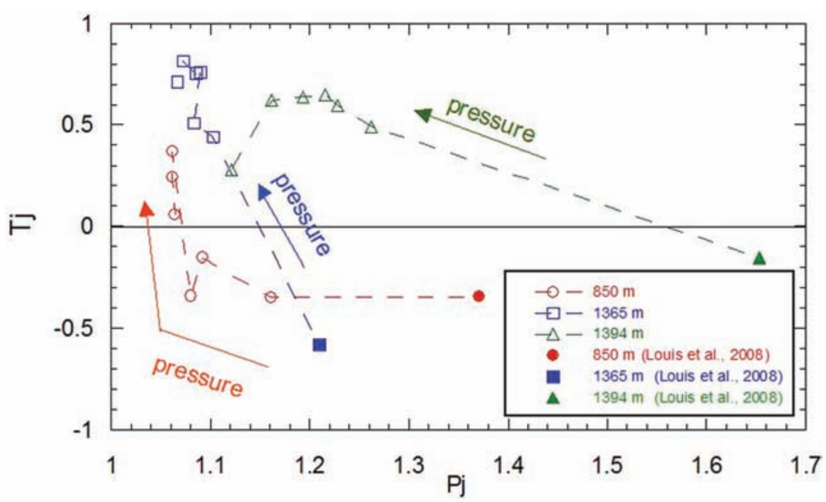

Figure 7. T_j versus P_j plot in the three samples showing the evolution of the shape of the velocity tensor ellipsoid.

although the maximum and minimum velocity directions obtained on the spheres were not geometrically constrained, the maximum velocity directions were observed in Fig. 5 to lay within the plane perpendicular to the minimum velocity direction, along with the ones obtained using the tensor method.

An intrinsic limitation of our approach is the case where two high (respectively low) velocity zones coexist, a situation that cannot be accounted for by a second-order symmetric tensor. However, among all the sample/pressure configurations studied here (Figs 4a and b), only one might correspond to this limiting case (sample at

850 m and 50 MPa), an interpretation of which is provided in the following.

4.2 Pressure dependence of *P*-wave velocity and inferred crack densities

The most remarkable observation made when mapping the 3-D velocity anisotropies in Figs 4(a) and (b) is that, for every sample, the direction of the minimum value remains very stable across all pressure steps, and is in geometrical agreement with the network of subparallel microcracks already described by Louis *et al.* (2008) in the sandstone samples, as was checked in Fig. 5 by rotating the directions obtained at 5 MPa from both the directly measured extrema and the recalculated eigenvalues. This observation implies that the 'velocity (or elastic) fabric' corresponding to the network of parallel microcracks persists at high confinement, which might appear counter-intuitive since microcracks are generally expected to close early in the deformation process. The possibility that the anisotropy signal is influenced by lattice preferred orientation of constituent minerals (like phyllosilicates) is not ruled out. Even more surprising is the fact that the value of the shape parameter T_j globally increases with pressure, suggesting that the crack effect is enhanced throughout the process as the fabric becomes more planar (Fig. 7). The persistence of the microcrack-related velocity fabric may be explained by the recent findings of Humbert *et al.* (2011). In that study, the authors employed a series of magnetic anisotropy measurement techniques to investigate a possible magnetic signature of the same TCDP sandstone microcracks. They were able to propose that (1) the vertical microcracks had been coated by a late generation of magnetite grains, and that (2) these microcracks however were not sealed, and therefore were likely to remain open at depth. If the microcracks are coated by neocrystallizations of micron-sized hard cubic crystals, it becomes much more difficult for the applied pressure to achieve complete closure, allowing the persistence of a high compliance direction normal to the plane of the microcracks.

Our data set on directional *P*-wave velocities measured under increasing pressure permits to estimate the so-called crack density tensor and its variation with pressure. Two different approaches were used, both of them based on the work of Sayers & Kachanov (1995). First, we applied a numerical inversion scheme described by Fortin *et al*. (2011), secondly we calculated the analytical solution proposed by Wong & Zhu (2007). To do so several assumptions had to be made to make the calculations easier. First, we assume that the velocity distribution in space is transversely isotropic with a symmetry axis corresponding to the direction of minimum velocity (which is close to the bedding strike). This assumption is not supported by the results of Louis *et al*. (2008) who found a 'triaxial' distribution of clustered eigenvectors (Fig. 5): however if we look at the distribution of maximum and intermediate principal axes derived from this study, we observe that these axes are scattered in a plane roughly orthogonal to the bedding strike, in agreement with what would be observed in the case of transversely isotropic symmetry. Given this assumption it is possible to calculate the elastic parameters $C_{11}^{\exp}$ and $C_{33}^{\exp}$ (in the simplified Voigt notation) from the measured maximum and minimum *P*-wave velocities at each pressure step ($C_{11}^{\exp} = \rho V_{\max}^2$ and $C_{33}^{\exp}=\rho V_{\min}^2$). The second assumption is that there are two populations of cracks in the rock, one considered to be isotropic with crack density $\rho_{\rm iso}$, and a second one made of parallel cracks oriented perpendicular to the bedding strike as shown by the study of Louis *et al*. (2008), with a crack density $\rho_{\rm v}$ ('v' is for vertical as the crack planes are subvertical).

The first method is based on the numerical scheme proposed by Fortin *et al*. (2011). The compliance tensor of the sandstone can be written as: $S_{ijkl} = S_{ijkl}^o + \Delta S_{ijkl}$, where S_{ijkl}^o is the compliance tensor of the crack free solid matrix, and ΔS_{ijkl} is the additional compliance resulting from the presence of cracks. Here, we will restrict our attention to the case when the rock matrix is isotropic, so that its elastic stiffness can be specified in terms of the Young's modulus E_o and Poisson's ratio ν_o. To model the additional compliance, ΔS_{ijkl}, we consider the case of a medium containing circular cracks. Thus, a crack density,ρ, can be defined as $\rho = \frac{1}{V}\sum_0^N c_i^3$, where c_i is the radius of the *i*th crack and N is the total number of cracks embedded in the representative volume V (Bristow 1960, Walsh 1965). In sandstones, microcracks are the result of imperfectly bonded interfaces at grain boundaries. These cracks may not be circular, but can be considered in a first approximation as flat cracks (Schoenberg 1980). In this case, the distribution of cracks of irregular shapes can be replaced by an equivalent distribution of circular cracks. Thus, the crack density as defined above is an effective density of the equivalent distribution of the circular cracks (Sevostianov & Kachanov 2002, Guéguen & Kachanov 2011). This parameter, ρ, is adequate for the isotropic case of randomly oriented cracks but cannot be used for other distributions of crack orientation. Following the work of Kachanov (1980), the scalar crack density, ρ, can be generalized to a second crack density tensor, $\boldsymbol{\alpha}$, defined as: $\boldsymbol{\alpha} = \frac{1}{V}\sum (c^3\mathbf{nn})^i$, where $\mathbf{n}$ is the unit vector normal to a crack, and $\mathbf{nn}$ is the dyadic product. The linear invariant $\alpha_{kk} = \rho$ so that $\boldsymbol{\alpha}$ is a natural tensorial generalization of ρ.

In the case, where contributions of cracks are evaluated in the non-interaction approximation (NIA)—without accounting for the interaction between cracks—the additional compliance, ΔS_{ijkl}, due to multiple circular cracks in arbitrary orientational distribution is given by Kachanov (1980), as

$$\Delta S_{ijkl} = h\left(\frac{1}{4}\left(\delta_{ik}\alpha_{jl} + \delta_{il}\alpha_{jk} + \delta_{jk}\alpha_{il} + \delta_{jl}\alpha_{ik}\right) - \frac{\nu_o}{2}\beta_{ijkl}\right), \quad (5)$$

where δ_{ij} is the Kronecker delta and h, a scalar defined as $h = \frac{32(1-\nu_0^2)}{3(2-\nu_0)E_o}$. Eq. (5) shows that the additional compliance is expressed as a function of the second-order crack density tensor $\boldsymbol{\alpha}$, but also as a function of a fourth rank tensor $\boldsymbol{\beta}$, defined as : $\boldsymbol{\beta} = \frac{1}{V}\sum (c^3\mathbf{nnnn})^i$. However as discussed by Sayers & Kachanov (1995) and Guéguen & Kachanov (2011), the fourth rank tensor will be small and in most rocks Poisson's ratio $\nu_o << 2$, thus neglecting the $\boldsymbol{\beta}$-term and retaining α as the sole crack density parameter usually constitutes a good approximation, especially in the case of a dry rock.

If we focus on a transversely isotropic rock (with symmetry axis x_3) associated with an axisymmetric distribution of microcracks embedded in an isotropic elastic matrix, then the symmetry condition necessarily requires that $\alpha_{11} = \alpha_{22}$. Using the Voigt notation the non-vanishing components of the elastic compliance of a cracked rock are given by

$$S_{11} = S_{22} = \frac{1}{E_o} + h\alpha_{11}, \quad (6a)$$

$$S_{33} = \frac{1}{E_o} + h\alpha_{33}, \quad (6b)$$

$$S_{44} = \frac{1}{G_o} + h\left(\alpha_{11} + \alpha_{33}\right), \quad (6c)$$

$$S_{66} = \frac{1}{G_o} + 2h\alpha_{11}, \tag{6d}$$

$$S_{12} = S_{13} = S_{23} = -\frac{\nu_0}{E_o}, \tag{6e}$$

where G_0 is the shear modulus of the crack-free matrix. The elastic stiffness of a cracked rock C_{11} and C_{33}, in the Voigt notation, are deduced using $C_{ij} = (S_{ij})^{-1}$ and

$$C_{11} = \left(S_{12}^2 - S_{11}S_{33}\right)/D \tag{7a}$$

$$C_{33} = \left(S_{12}^2 - S_{11}^2\right)/D \tag{7b}$$

with $D = S_{12}^2(2S_{11} + S_{33}) - S_{33}S_{11}^2 - 2S_{12}^3$. The eqs. (6a)–(6e) are valid, in the case of transversely isotropic symmetry for any arbitrary distributions of cracks. For a medium containing randomly oriented cracks, the elastic compliance can be simplified using $\alpha_{11} = \alpha_{22} = \alpha_{33}$. However, as it can be seen from Fig. 6, *P*-wave velocity anisotropy exists with a minimum value in the direction of the symmetry axis x_3. This implies $\alpha_{11} \neq \alpha_{33}$ and $\alpha_{33} \geq \alpha_{11}$. Thus, to interpret the second crack density tensor $\boldsymbol{\alpha}$ in terms of microstructural attributes, it is possible to rewrite $\boldsymbol{\alpha}$ as:

$$\boldsymbol{\alpha} = \alpha_{11}\mathbf{I} + (\alpha_{33} - \alpha_{11})\mathbf{e_3}\mathbf{e_3}, \tag{8}$$

where $\mathbf{I}$ is the unit tensor, and $\mathbf{e_3}$ the unit vector along the x_3 axis. The difference $\rho_v = \alpha_{33} - \alpha_{11}$ characterizes the crack density of parallel cracks with normal along (Ox_3), whereas the tensor $\alpha_{11}\mathbf{I}$ characterizes cracks randomly oriented with a crack density $\rho_{\text{iso}} = 3\alpha_{11}$. As a consequence, the elastic compliance of a cracked rock (eqs 6a–6e) can be rewritten as a function of these two crack densities, ρ_{iso} and ρ_v, using $\alpha_{11} = \frac{\rho_{\text{iso}}}{3}$ and $\alpha_{33} = \frac{\rho_{\text{iso}}}{3} + \rho_v$.

Finally, the theoretical prediction of the effective medium model provided by eqs (7) and (6) in terms of effective stiffness C_{11} and C_{33} are compared to the elastic stiffness $C_{11}^{\exp}$ and $C_{33}^{\exp}$ obtained from the elastic wave velocities measurements, and the distance between them is defined by a least-square function F given by $F = (C_{11}^{\exp} - C_{11})^2 + \left(C_{33}^{\exp} - C_{33}\right)^2$ that needs to be minimized at each loading stage with respect to the unknown variables ρ_{iso} and ρ_v.

In the second method we used Wong & Zhu's (2007) analytical solution for weakly anisotropic cracked rocks, which was also based on Kachanov's (1980) formulation. In particular, their eq. (10a) gives the following expression for one of Thomsen's (1986) anisotropy parameters

$$\begin{aligned}\varepsilon &= \frac{C_{11} - C_{33}}{2C_{33}} = \frac{E_o h}{2}\frac{(\alpha_{33} - \alpha_{11})(1 + E_o h\alpha_{11})}{\left[(1 + E_o h\alpha_{11})^2 - \nu_o^2\right]} \\ &= \frac{E_o h}{2}\frac{\rho_v\left(1 + E_o h\rho_{iso}/3\right)}{\left[\left(1 + E_o h\rho_{iso}/3\right)^2 - \nu_o^2\right]}\end{aligned} \tag{8a}$$

It should be noted that our two crack density parameters $\rho_{\text{iso}} = 3\alpha_{11}$ and $\rho_v = \alpha_{33} - \alpha_{11}$ here correspond to the parameters *a* and *b* defined by Wong & Zhu (2007). Since we typically have $\upsilon_0^2 \leq 1$, the above can be approximated by:

$$\varepsilon = \frac{C_{11} - C_{33}}{2C_{33}} \approx \frac{E_o h}{2}\frac{\rho_v}{\left(1 + E_o h\rho_{\text{iso}}/3\right)} \tag{8b}$$

Substituting eq. (6) into eq. (7b), we can also obtain:

$$\begin{aligned}\frac{C_{33}}{E_o} &= \frac{(1 - \nu_o + E_o h\rho_{\text{iso}}/3)}{(1 + E_o h(\rho_{\text{iso}}/3 + \rho_v))(1 - \nu_o + E_o h\rho_{\text{iso}}/3) - 2\nu_o^2} \\ &\approx \frac{1}{(1 + E_o h(\rho_{iso}/3 + \rho_v))}.\end{aligned} \tag{9}$$

Solving the above simultaneous equations, we arrive at these analytic expressions for the two crack density parameters (and corresponding ratio) in terms of the measured velocities (and corresponding elastic stiffnesses and Thomsen parameter ε)

$$\rho_{\text{iso}} \approx \frac{3}{E_o h}\left[\frac{E_o/C_{33}}{(1 + 2\varepsilon)} - 1\right] \tag{10a}$$

$$\rho_v \approx \frac{2}{E_o h}\frac{\varepsilon}{1 + 2\varepsilon}\frac{E_o}{C_{33}} \tag{10b}$$

$$\frac{\rho_v}{\rho_{iso}} \approx \frac{2}{3}\varepsilon\left[\frac{(E_o/C_{33})}{(E_o/C_{33}) - (1 + 2\varepsilon)}\right]. \tag{10c}$$

It is of interest to note that this ratio is independent of the Poisson's ratio, and the crack anisotropy is manifested by coupled effects on the normalized stiffness and Thomsen's parameter.

In Fig. 8(a) we plotted the results for the numerical model, and in Fig. 8(b) the results given by the analytical solution, for the pressure dependence of both crack densities. For the calculation we took $E_o = 51$ GPa, $\nu_o = 0.2$ and a bulk density of 2240 kg m^{-3} (Louis *et al*. 2008). The input data for the inversion were the minimum and maximum measured *P*-wave velocities. The first striking observation is that both methods give almost the same results, which in a sense validates the numerical approach. The only visible difference is at the highest confining pressure where the analytical solution predicts smaller values for the crack density of the isotropic population. This will have some consequences as discussed below. The second striking observation is that at low pressure, the crack densities reach relatively high values: this is in agreement with the microstructural analysis conducted by Louis *et al*. (2008) who observed that most of the grains in their sandstone samples were cracked (see their fig. 12 in Louis *et al*. 2008). As expected both crack densities ρ_{iso} and ρ_{v} decrease significantly with increasing pressure, but the amplitude of the decrease is not the same for both distributions. Indeed, the isotropic crack density has a sharper decrease compared to the anisotropic one which becomes almost constant after applying 50 MPa confining pressure. The inserted graphs in Fig. 9 represent the evolution of the crack density ratio $\rho_{\text{v}}/\rho_{\text{iso}}$ as a function of confining pressure. The small discrepancy at high pressure in crack density for the isotropic distributions especially in samples at 1394 m and 1365 m has a significant impact on the crack density ratio and the shape of the curves are slightly different. Nevertheless the important result is that in both cases the crack density ratio increases with pressure, providing quantitative estimates on the contrasting behaviours of vertical and randomly oriented sets of microcracks: as the pressure is increasing, the influence of crack anisotropy becomes relatively more important. Consequently we expect that the elastic fabric becomes more and more planar. Nevertheless reminding that the measurements have been done on dry samples, one should be cautious in extrapolating the results to rocks under *in situ* conditions where fluids are present in cracks and pores.

4.3 Evidence for higher order of anisotropy

The analysis in Section 4.2 was done assuming a transversely isotropic symmetry for the elastic fabric. Actually this assumption is not in complete agreement with our data set as three independent clustered velocity axes are found. In fact, it is possible that additional anisotropic features are present in the tested samples. The increase in the value of T_j, at least up to 50 MPa of applied pressure, may in fact be associated with the transition from one (or a combination of) anisotropy source(s) to another. In Section 3.3, we pointed out the tendency for T_j to also decrease slightly for the highest pressure steps, and suggested for the sample at 850 m and 50 MPa that this behaviour might reflect a displacement of the maximum velocity sector in Figs 4(a) and (b). To obtain such a substitution, it is necessary that (1) several sources of anisotropy are present and that (2) these sources exhibit different pressure sensitivities. Louis *et al.* (2008) interpreted the orientation of the eigenvectors as resulting from a combination of vertical microcracks anisotropy and bedding anisotropy. The maximum velocity would be found at the geometric intersection between these two features (i.e. within both the plane of microcracks and the bedding plane). The concept of the maximum velocity direction lying parallel to the intersection direction of two fabric elements has also been described by Healy *et al*. (2009) and Lloyd *et al*. (2009) with combinations of cracks and ductile fabric elements. We saw in the present work that the velocity anisotropy deviates from this pattern as pressure rises. Indeed, although the minimum velocity tends to remain in the same location, the maximum velocity travels within the plane transverse to the minimum direction and is not systematically found at the intersection between the microcracks and the bedding plane (Fig. 5). In an early comparison between elastic and magnetic anisotropies in rock samples from the Bohemian Massif in Czech Republic, Hrouda *et al.* (1993) inferred the presence in a set of undeformed samples of bed parallel cracks potentially formed during erosion and uplift. Alternately, such microcracks may also simply form as collateral to the coring process. We suggest that the anisotropy associated with the bedding in our sandstone samples be due to intergranular microcracks

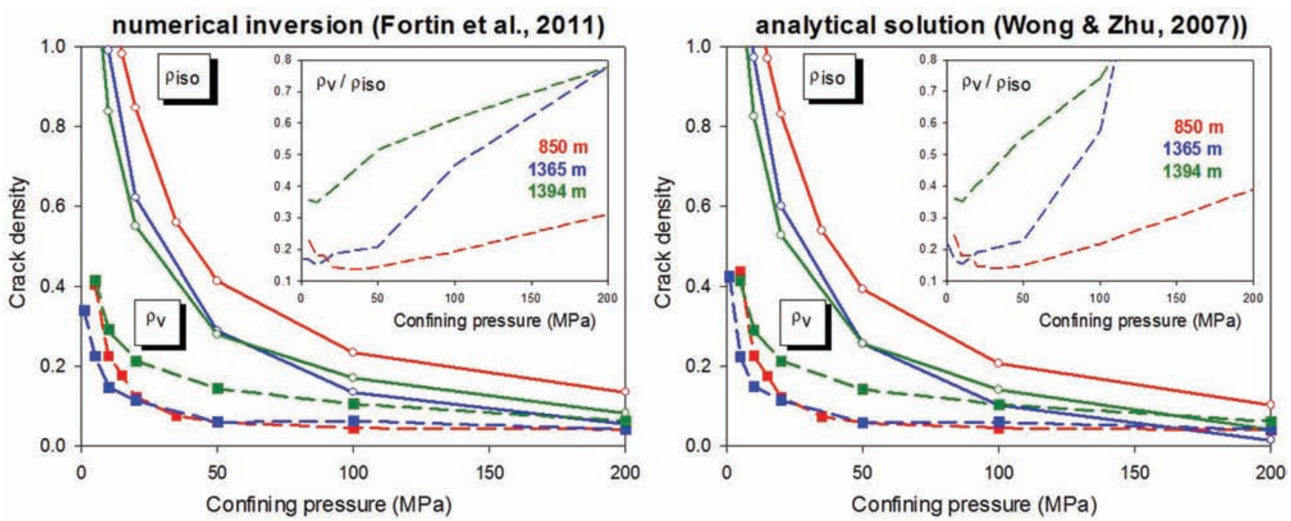

Figure 8. Crack densities estimated using the Sayers & Kachanov (1995) scheme as a function of applied confining pressure. Inserted is a plot of the crack density ratio between the isotropic and the anisotropic crack distributions. (a) Predictions of the numerical scheme proposed by Fortin *et al*. (2011) (b) Predictions derived from the analytical solution of Wong & Zhu (2007).

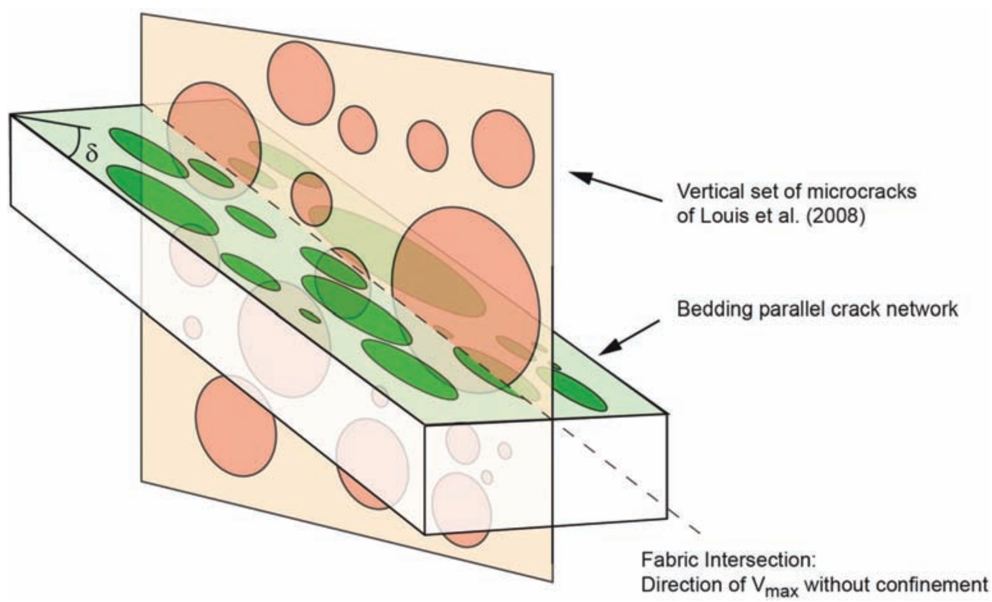

Figure 9. Conceptual model showing two different contributions to the rock anisotropy associated with cracks either vertical or parallel to the bedding plane.

that can close more readily than the partially filled vertical ones. Such bed parallel microcracks possibly related to cleavage planes in phyllosilicates would be difficult to identify in the microstructures as opposed to intragranular ones. This scheme, which refines the one proposed by Louis *et al.* (2008) by adding a pressure sensitive component to the velocity anisotropy, is illustrated in Fig. 9. In the absence of confining stress, both sources of anisotropy (bed parallel and vertical microcracks) cause the maximum *P*-wave velocity to be observed along the intersection between the two planes. As the pressure rises, the bedding parallel cracks readily close, causing the maximum velocity direction to be released from the intersection direction and scattered into the plane transverse to the minimum velocity direction.

ACKNOWLEDGMENTS

We thank Veronika Vajdova who initiated the contacts with Petr Špaček. The research at Stony Brook was partially supported by the USGS National Earthquake Hazards Reduction Program (Grants #05HQGR0065 and 06HQGR0030). Petr Špaček was funded by ESF/MEYS project CZ.1.07/2.3.00/20.0052 'Research group for radioactive waste repository and nuclear safety'. M. Machek and L. Padjen are thanked for technical assistance. Many thanks to both reviewers Mark Kachanov and Dave Healy for their comments which helped to improve the paper.

REFERENCES

Arts, R.J., Rasolofosaon, N.P. & Zinszner, B.E., 1994. Experimental and theoretical tools for characterizing anisotropy due to mechanical defects in rocks under varying pore and confining pressures, in *Transactions 6th Int. Workshop on Seismic Anisotropy,* pp. 1–33, eds. Fjaer, E., Holt, M., & Rathore, J.S., SEG, Tulsa, OK.

Borradaile, G.J. & Henry, B., 1997. Tectonic applications of magnetic susceptibility and its anisotropy, *Earth Sci. Rev.,* **42,** 49–93.

Bristow, J., 1960. Microcracks and the static and dynamic constants of annealed and heavily cold-worked metals. *J. appl. Phys.,* **11,** 81–85.

Crampin, S., 1981. A review of wave motion in anisotropic and cracked elastic-media, *Wave Motion,* **3,** 343–391.

David, C., Robion, P. & Menéndez, B., 2007. Anisotropy of elastic, magnetic and microstructural properties of the Callovo-Oxfordian argillite, *Phys. Chem. Earth,* **32,** 145–153.

Fortin, J., Stanchits, S., Vinciguerra, S. & Guéguen, Y., 2011. Influence of thermal and mechanical cracks on permeability and elastic wave velocities in a basalt from Mt. Etna volcano subjected to elevated pressure, *Tectonophysics,* **503,** 60–74.

Guéguen, Y. & Kachanov, M., 2011. Effective elastic properties of cracked and porous rocks – an overview, in *Mechanics of Crustal Rocks*, CISM International Centre for Mechanical Sciences Vol. 533, eds Leroy, Y. M. & Florian, K., Springer, Berlin, in press.

Healy, D., Reddy, S.M., Timms, N.E., Gray, E.M. & Vitale Brovarone, A. 2009. Trench-parallel fast axes of seismic anisotropy due to fluid-filled cracks in subducting slabs, *Earth planet. Sci. Lett.,* **283,** 75–86.

Helbig, K. & Thomsen, L., 2005. 75-plus years of anisotropy in exploration and reservoir seismics: a historical review of concepts and methods, *Geophysics,* **70,** doi:10.1190/1.2122407.

Hornby, B.E., 1998. Experimental laboratory determination of the dynamic elastic properties of wet, drained shales, *J. geophys. Res.,* **103,** 29 945–29 964.

Hrouda, F., Zdenek, P. & Wohlgemuth, J. 1993. Development of magnetic and elastic anisotropies in slates during progressive deformation. *Phys. Earth planet. Inter.,* **77,** 251–265.

Humbert, F., Robion, P., Louis, L., Bartier, D., Ledésert, B. & Song, S.-R., 2011. Magnetic inference of *in situ* open microcracks in sandstone samples from the Taiwan Chelungpu Fault Drilling Project (TCDP). *J. Asian Earth Sci.,* in press.

Jelinek, V., 1981. Characterization of the magnetic fabrics of rocks, *Tectonophysics,* **79,** 63–67.

Johnston, J.E. & Christensen, N.I., 1995. Seismic anisotropy of shales, *J. geophys. Res.,* **100,** 5991–6003.

Kachanov, M., 1980. Continuum model of medium with cracks. *J. Eng. Mech. Div., ASCE* **106**(EM5), 1039–1051.

Kern, H., 1993. P- and S-wave anisotropy and shear-wave splitting at pressure and temperature in possible mantle rocks and their relation to the rock fabric, *Phys. Earth planet. Inter.,* **78,** 245–256.

Lloyd, G.E., Butler, R.W.H., Casey, M. & Mainprice, D., 2009. Mica, deformation fabrics and the seismic properties of the continental crust, *Earth planet. Sci. Lett.,* **288,** 320–328.

Lo, T.W., Coyner, K.B. & Toksoz, M.N., 1986. Experimental determination of elastic anisotropy of Berea Sandstone, Chicopee Shale, and Chelmsford Granite, *Geophysics,* **51,** 164–171.

Louis, L., Chen, N.T.M., David, C., Robion, P., Wong, T.F. & Song, S.R., 2008. Anisotropy of magnetic susceptibility and P-wave velocity in core samples from the Taiwan Chelungpu-Fault Drilling Project (TCDP), *J. Struct. Geol.,* **30,** 948–962.

Louis, L., David, C. & Robion, P., 2003. Comparison of the anisotropic behaviour of undeformed sandstones under dry and saturated conditions, *Tectonophysics,* **370,** 193–212.

Louis, L., Robion, P. & David, C., 2004. A single method for the inversion of anisotropic data sets with application to structural studies, *J. Struct. Geol.,* **26,** 2065–2072.

Machek, M., Špaček P., Ulrich, S. & Heidelbach F., 2007. Origin and orientation of microporosity in eclogites of different microstructure studied by ultrasound and microfabric analysis, *Eng. Geol.,* **89,** 266–277.

Mavko, G., Mukerji, T. & Dvorkin, J., 1998. *The Rock Physics Handbook,* Cambridge University Press, Cambridge, 329pp.

Nur, A. & Simmons, G., 1969. Stress-induced velocity anisotropy in rock: an experimental study, *J. geophys. Res.,* **74,** 6667–6674.

Nye, J.F., 1957. *Physical Properties of Crystals – Their Representation by Tensors and Matrices,* Oxford Science Publications, Oxford.

Pros, Z., Lokajíček, T. & Klíma, K., 1998a. Laboratory approach to the study of elastic anisotropy on rock samples, *Pageoph,* **151,** 619–629.

Pros, Z., Lokajíček, T., Přikryl, R., Špičák, A., Vajdová V. & Klíma K., 1998b. Elastic parameters of West Bohemian granites under hydrostatic pressure, *Pageoph,* **151,** 631–646.

Pros, Z., Lokajíček, T., Přikryl, R. & Klíma, K. 2003. Direct measurement of 3D elastic anisotropy on rocks from the Ivrea zone (Southern Alps, NW Italy), *Tectonophysics,* **370**(1–4), 31–47.

Rasolofosaon, N.P.J., Rabbel, W., Siegesmund, S. & Vollbrecht, A., 2000. Characterization of crack distribution: fabric analysis versus ultrasonic inversion, *Geophys. J. Int.,* **141,** 413–424.

Rasolofosaon, N.P.J. & Zinszner, B.E., 2002. Comparison between permeability anisotropy and elasticity anisotropy of reservoir rocks, *Geophysics,* **67,** 230–240.

Sayers, C.M. & Kachanov, M., 1995. Microcrack-induced elastic wave anisotropy of brittle rocks, *J. geophys. Res.,* **100,** 4149–4156.

Schoenberg, M., 1980. Elastic wave behaviour across linear slip interfaces, *J. acoust. Soc. Am.,* **68**(5), 1516–1521.

Sevostianov, I. & Kachanov, M., 2002. On elastic compliances of irregularly shaped cracks, *Int. J. Fract.,* **114,** 245–257.

Sevostianov, I. & Kachanov, M., 2008. On approximate symmetries of the elastic properties and elliptic orthotropy, *Int. J. Eng. Sci.,* **46,** 211–223.

Shin, T.C. & Teng, T.L., 2001. An overview of the 1999 Chi-Chi, Taiwan, earthquake, *Bull. seism. Soc. Am.,* **91,** 895–913.

Song, S.R., Wang, C.Y., Hung, J.H. & Ma, K.F., 2007. Preface to the special issue on Taiwan Chelungpu-fault Drilling Project (TCDP): site characteristics and on-site measurements. *Terr. Atmos. Oceanic Sci.,* **18**(2), I–V.

Tarling, D.H. & Hrouda, F., 1993. *The Magnetic Anisotropy of Rocks*. Chapman and Hall, London, 217 pp.

Thomsen, L., 1986. Weak elastic anisotropy, *Geophysics,* **51**(10), 1954–1966.

Tsvankin, I., 1997. Anisotropic parameters and P-wave velocity for orthorhombic media, *Geophysics,* **62**(4), 1292–1309.

Vajdová, V., Přikryl, R., Pros, Z. & Klíma, K., 1999. The effect of rock fabric on P-wave velocity distribution in amphibolites, *Phys. Earth planet. Inter.,* **114,** 39–47.

Vilhelm, J., Rudajev, V., Živor, R., Lokajíček, T. & Pros, Z., 2008. Comparison of field and laboratory seismic velocity anisotropy measurement (scaling factor), *Acta Geodyn. Geomater.,* **5**(2), 161–169.

Walsh, J., 1965. The effect of cracks on the compressibility of rocks, *J. geophys. Res.,* **70,** 381–389.

Wong, T.f. & Zhu, W., 2007. Weak elastic anisotropy in a cracked rock, *Geol. Soc. Lond. Spec. Pub.,* **284,** 207–220, doi:10.1144/SP284.14.